Morphology and electrochemical performance of Li[Li$_{0.2}$Mn$_{0.54}$Ni$_{0.13}$Co$_{0.13}$]O$_2$ cathode materials treated in molten salts

S.J. Shi, J.P. Tu*, Y.Y. Tang, X.Y. Liu, X.Y. Zhao, X.L. Wang, C.D. Gu

State Key Laboratory of Silicon Materials, Key Laboratory of Advanced Materials and Applications for Batteries of Zhejiang Province, Department of Materials Science and Engineering, Zhejiang University, Hangzhou 310027, Zhejiang, China

HIGHLIGHTS

- Cube and plate-like particles are obtained after treated in LiCl and KCl molten salts.
- Oxide treated in KCl molten salt has large specific area of 17.05 m^2 g^{-1}.
- And discharge capacity of 168.5 mAh g^{-1} is obtained at 10 C.
- Oxide treated in LiCl molten salt has enhanced capacity retention of 94.9%.

ARTICLE INFO

ABSTRACT

Cube-like and plate-like Li[Li$_{0.2}$Mn$_{0.54}$Ni$_{0.13}$Co$_{0.13}$]O$_2$ particles are obtained after treated in LiCl and KCl molten salts at 800 °C, respectively, comparing to the ball-like original particles calcined in air. The oxide treated in KCl molten salt with large specific area of 17.05 m^2 g^{-1} delivers high discharge capacities of 254.1 mAh g^{-1} and 168.5 mAh g^{-1} at current densities of 200 mA g^{-1} and 2000 mA g^{-1}, respectively. In addition, enhanced cycle stability with capacity retention of 94.9% after 80 cycles at charge−discharge current densities of 200 mA g^{-1} is obtained for the oxide treated in LiCl molten salt with sacrifice of a little capacity. Such electrochemical performance change is proved to be independent of Li$^+$ diffusion coefficient. It appears that the treatment in molten salts can effectively reform the electrochemical performances of Li[Li$_{0.2}$Mn$_{0.54}$Ni$_{0.13}$Co$_{0.13}$]O$_2$ cathode materials for various applications.

© 2013 Elsevier B.V. All rights reserved.

1. Introduction

Lithium ion batteries have been widely applied as energy storage for mobile electronic devices due to their high energy density, long cycle life and high security. With the development of electric vehicles and hybrid vehicles, new-generation cathode materials with higher specific capacity should be urgently explored to replace LiCoO$_2$ for application [1−10]. Recently, a material design which adds extra lithium, manganese, and charge-compensating oxygen into LiMn$_x$Ni$_y$Co$_z$O$_2$ resulting in the formation of Li$_2$MnO$_3$-like regions to stabilize the electrode structure and enhance the discharge capacity by extracting the lithium concomitant with release of oxygen (a net loss of Li$_2$O) to form a layered MnO$_2$ component has been performed to obtain Li-rich layered cathode materials with a notation of xLi$_2$MnO$_3$·(1 − x)LiMO$_2$ (M = Mn, Ni, Co) [11−15].

Among them, Li[Li$_{0.2}$Mn$_{0.54}$Ni$_{0.13}$Co$_{0.13}$]O$_2$, which can be rewritten in two-component notation as 0.5Li$_2$MnO$_3$·0.5LiNi$_{1/3}$Co$_{1/3}$Mn$_{1/3}$O$_2$, attracts the attentions as one of the most promising candidates for lithium ion batteries [3,16−20]. As reported, Li[Li$_{0.2}$Mn$_{0.54}$Ni$_{0.13}$Co$_{0.13}$]O$_2$ cathode could deliver an initial discharge capacity above 250 mAh g^{-1} when discharged from 4.8 to 2.0 V at 12.5−20 mA g^{-1} at room temperature [13,16,20,21]. Many methods and processes have been recently developed to prepare high quality Li[Li$_{0.2}$Mn$_{0.54}$Ni$_{0.13}$Co$_{0.13}$]O$_2$ materials, such as co-precipitation [3,16−21], sol−gel process [22−24], combustion method [25−27].

The molten salt synthesis process uses a molten salt as a media for the constituent oxides, which enables molecular level mixing of different reactants, and thus leads to a homogenous structure of the final product [28]. LiCl and KCl are both non-oxidizing flux but act as an excellent 'mineralizing' agent to give well-crystalline oxides [28−32]. They have already been used to synthesize cathode materials such as LiCoO$_2$ [29], LiFePO$_4$/C [33], LiMn$_2$O$_4$ [34], LiNi$_{1/3}$Co$_{1/3}$Mn$_{1/3}$O$_2$ [32], LiNi$_{0.8}$Co$_{0.1}$Mn$_{0.1}$O$_2$ [30], and so on. Usually, the mixtures such as acetates, nitrates, transition metal oxides or

* Corresponding author. Tel.: +86 571 87952856; fax: +86 571 87952573.
  E-mail addresses: tujp@zju.edu.cn, tujplab@zju.edu.cn (J.P. Tu).

hydroxide and Li source react in the molten salt at high temperatures to form final cathode materials. Easy heat and material transfer significantly reduces the forming time and decreases the anneal temperature with better crystallinity. Furthermore, particles with specific shape could be obtained due to the as-used molten salt media which might affect the particle growth or the reactions between the precursor and Li source of the layered oxides [30]. In addition, because of the good water solubility of alkali chloride, it is easy to remove the excess alkali chloride from the mixture to obtain pure layered oxides.

Here, we use LiCl and KCl molten salts, respectively, to control the particle growth of layered oxide $Li[Li_{0.2}Mn_{0.54}Ni_{0.13}Co_{0.13}]O_2$. The control process is carried out after the Li-rich layered oxide is primarily formed by combustion at 500 °C with alcohol as fuel which is different from normal molten salt synthesis. Interesting results are obtained after the particles growing in air, LiCl and KCl molten salts, respectively. The morphology and electrochemical performance of $Li[Li_{0.2}Mn_{0.54}Ni_{0.13}Co_{0.13}]O_2$ are different after treated in the salts. It offers a promising method to control the particle growth of Li-rich layered oxides with different molten salts to obtain the ideal cathode materials for applications.

2. Experimental

The precursor is synthesized by alcohol assisted combustion method in our previous work [27]. Stoichiometric amounts of $LiNO_3$ (8.52 g), $Ni(NO_3)_2 \cdot 6H_2O$ (3.78 g), $Co(CH_3COO)_2 \cdot 4H_2O$ (3.24 g) and $Mn(CH_3COO)_2 \cdot 4H_2O$ (13.23 g) were dissolved in 40 ml alcohol. Among them, 3 wt.% excess Li source was added to compensate the lost during calcination treatment. Fierce stir was performed until a transparent solution was obtained. The resulting solution was poured into a 300 ml corundum crucible. The crucible was put into a chamber furnace which was pre-heated to 500 °C in air. The combustion reaction finished less than 5 min. Then, the combustion product was ground in a carnelian mortar and mixed thoroughly with LiCl and KCl, respectively. The mixtures were again treated in molten salts at 800 °C for 16 h to get the layered oxide Li [$Li_{0.2}Mn_{0.54}Ni_{0.13}Co_{0.13}]O_2$. After cooling to room temperature, the mixtures were washed by deionized water for several times to remove the excess salts thoroughly, and dried at 120 °C over night. The as-synthesized oxides were named as $Li[Li_{0.2}Mn_{0.54}Ni_{0.13}Co_{0.13}]$ $O_2/LiCl$ and $Li[Li_{0.2}Mn_{0.54}Ni_{0.13}Co_{0.13}]O_2/KCl$ for short. In addition, the combustion product was also calcined at 800 °C in air for 16 h to get the bare $Li[Li_{0.2}Mn_{0.54}Ni_{0.13}Co_{0.13}]O_2$.

The element amount was analyzed by inductively coupled plasma emission spectrometer (ICP, IRIS Intrepid II). The morphologies and structures of the as-synthesized powders were characterized using field emission scanning electron microscopy (FESEM, S-4800), transmission electron microscopy (TEM, Tecnai G2 F30 S-Twin) and X-ray photoelectron spectroscopy (XPS, PHI 5700). XRD measurements were collected on a Rigaku D/Max-2550pc X-ray diffractometer, using CuKα radiation at 40 kV and 250 mA from 2θ degree of 10.0–80.0°, with an increasing step of 0.02° and counting duration of 1.0 s for each step. The specific surface areas of the powders were measured following the multipoint Brunauer–Emmett–Teller (BET) procedure from the N_2 adsorption–desorption isotherms using an AUTOSORB-1-C gas sorption analyzer.

The working electrodes were prepared by a slurry coating procedure. The slurry consisted of 85 wt.% oxide powders, 10 wt.% carbon conductive agent and 5 wt.% polyvinylidene fluoride (PVDF) was coated on aluminum foil. After drying at 90 °C for 24 h in vacuum, the samples were pressed under a pressure of 20 MPa. A metallic lithium foil served as the anode, 1 M $LiPF_6$ in ethylene carbonate (EC)–dimethyl carbonate (DMC) (1:1 in volume) was used as the electrolyte, and a polypropylene micro-porous film (Cellgard 2300) as the separator. The coin-type cells were assembled in an argon-filled glove box with H_2O concentration below 1 ppm. The galvanostatic discharge–charge tests were performed on a LAND battery program-control test system (Wuhan, China) between 2.0 and 4.8 V at the charge–discharge current densities from 20 to 2000 mA g^{-1} at room temperature. Galvanostatic intermittent titration technique (GITT) was also conducted on this apparatus at room temperature in the voltage range of 2.0–4.8 V. Cyclic voltammetry (CV) test was carried out on an electrochemical workstation (CHI660C) in the potential window of 2.0–5.0 V (vs. Li/ Li^+) at a scan rate of 0.1 mV s^{-1}. Electrochemical impedance spectroscopy (EIS) measurements were performed on this apparatus using a three-electrode cell with the layered oxides as the working electrode, metallic lithium foil as both the counter and reference electrodes. The amplitude of the AC signal was 5 mV over a frequency range from 100 kHz to 10 mHz at different charge states.

3. Results and discussion

3.1. Material characterization

Chemical analysis of the element amount in the oxides is performed by ICP–AES. The analytical results are $Li_{1.21}Mn_{0.54}Ni_{0.133}$-$Co_{0.129}O_2$, $Li_{1.22}Mn_{0.54}Ni_{0.129}Co_{0.128}O_2$ and $Li_{1.16}Mn_{0.54}Ni_{0.129}$ $Co_{0.134}O_2$ (Li/M = Mn + Ni + Co and Co, Ni/Mn) for $Li[Li_{0.2}Mn_{0.54}$-$Ni_{0.13}Co_{0.13}]O_2$, $Li[Li_{0.2}Mn_{0.54}Ni_{0.13}Co_{0.13}]O_2/LiCl$ and $Li[Li_{0.2}Mn_{0.54}$-$Ni_{0.13}Co_{0.13}]O_2/KCl$, respectively. The experimental Li contents are found a little deviate from the nominal composition. The least amount of Li in $Li[Li_{0.2}Mn_{0.54}Ni_{0.13}Co_{0.13}]O_2/KCl$ may be ascribed to the exchange with H^+ during repeated washing with de-ion water [35,36]. However, such low exchange amount with H^+ will not affect the intrinsic structure of the layered oxide apparently. XRD patterns of the oxides after the combustion reaction and further treated with or without molten salts are shown in Fig. 1. For all the XRD patterns, except the super-lattice peaks between 20° and 25°, the other peaks can be indexed the α-$NaFeO_2$ structure with space group R-3m. However, the diffraction peaks of the powder after combustion reaction at 500 °C without further calcination are weak and broad, and no distinct splitting (006)/(102) and (108)/(110) peaks are observed. It indicates that the combustion product has poor crystallinity and needs to be further calcined for high crystallinity and better hexagonal order. The weak peaks between 20° and 25° for the calcined products, as clearly shown in the right of Fig. 1(b), are consistent with the $LiMn_6$ cation arrangement that occurs in the transition metal layers of Li_2MnO_3 region or nanodomains, which can be indexed to the monoclinic unit cell C2/m [37,38]. No peak for any impurity phase is detected in these patterns, indicating high purity of the oxides without alkali chloride remained. In addition, after treated in the alkali chloride molten salts, the weak peaks with respect to the $LiMn_6$ cation arrangement become more symmetrical and sharper, especially for Li $[Li_{0.2}Mn_{0.54}Ni_{0.13}Co_{0.13}]O_2/LiCl$. The peak of (110) C2/m is separated from the serial peaks between 20° and 25°, indicating much better crystallinity of $Li[Li_{0.2}Mn_{0.54}Ni_{0.13}Co_{0.13}]O_2/LiCl$. It is reported that the single broad peak at 20.9° of the layered oxide synthesized at a relatively low temperature is attributed to an increase in the amount of stacking faults (shifting of the TM layers) [39]. The role of the stacking faults on the electrochemical performances of the cathode material is unclear. From thermodynamics, the introduction of stacking faults and other defects may increase the energy state of material, which can decrease the activation barrier for Li^+ diffusion and allow Li^+ to be extracted at a relatively low potential. Apparently, it will make the activation of the Li_2MnO_3 region during initial charge easier to some degree for bare Li
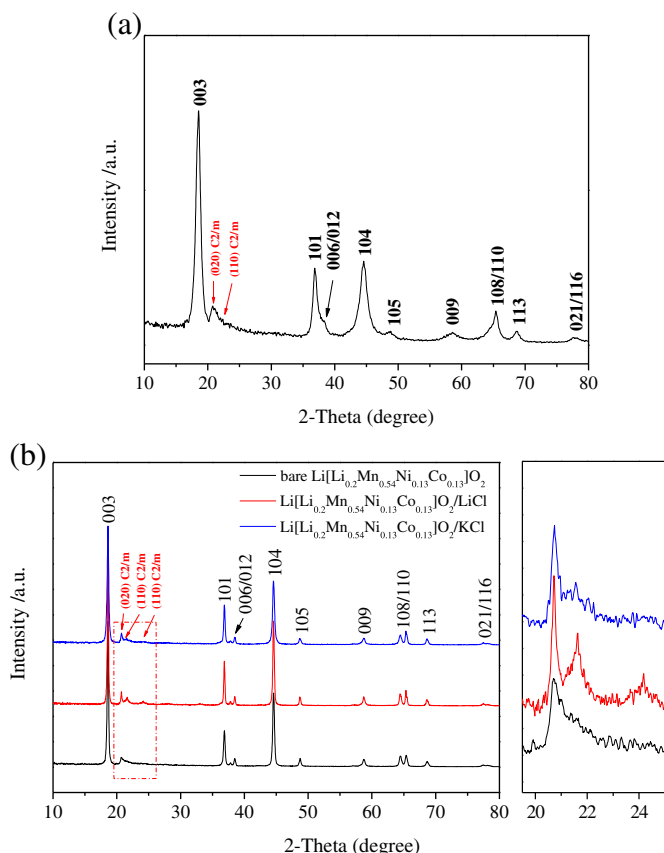
(a)

(b)

Fig. 1. XRD patterns of Li[Li$_{0.2}$Mn$_{0.54}$Ni$_{0.13}$Co$_{0.13}$]O$_2$ synthesized at 500 °C (a) without further heat treatment, and (b) treated with or without molten salt at 800 °C. The right part of (b) is the magnification of the XRD patterns from 20° to 25° in the red dashed. (For interpretation of the references to color in this figure legend, the reader is referred to the web version of this article.)

Fig. 2. SEM images of Li[Li$_{0.2}$Mn$_{0.54}$Ni$_{0.13}$Co$_{0.13}$]O$_2$ powders: (a) calcined in air, (b) treated in LiCl molten salt and (c) treated in KCl molten salt.

[Li$_{0.2}$Mn$_{0.54}$Ni$_{0.13}$Co$_{0.13}$]O$_2$ and Li[Li$_{0.2}$Mn$_{0.54}$Ni$_{0.13}$Co$_{0.13}$]O$_2$/KCl. However, the activation of the Li$_2$MnO$_3$ region of Li[Li$_{0.2}$Mn$_{0.54}$Ni$_{0.13}$Co$_{0.13}$]O$_2$/LiCl during initial charge becomes much more difficult according to the analysis of the XRD patterns. Further studies of these are in progress.

It has been reported that the ordering of the oxide structure can be indicated from the XRD patterns with the intensity ratios of I_{003}/I_{104} and $(I_{006} + I_{012})/I_{101}$ (R factor) and the degree of the (006)/(102) and (108)/(110) peak splitting [39,40]. The intensity ratio of I_{003}/I_{104} indicates the confusion of Li$^+$ and Ni^{+2} due to similar ion radii, and the smaller the R factor is, the better the hexagonal ordering is. All the oxides after treatment at 800 °C have distinct splitting of (006)/(102) and (108)/(110) peak. Likewise, the R factors of all the oxides are small. 0.2792, 0.2582 and 0.2253 for Li[Li$_{0.2}$Mn$_{0.54}$Ni$_{0.13}$Co$_{0.13}$]O$_2$, Li[Li$_{0.2}$Mn$_{0.54}$Ni$_{0.13}$Co$_{0.13}$]O$_2$/LiCl and Li[Li$_{0.2}$Mn$_{0.54}$Ni$_{0.13}$Co$_{0.13}$]O$_2$/KCl, respectively, indicating excellent hexagonal ordering after high temperature calcination no matter there is alkali chloride molten salts or not. Furthermore, the intensity ratios of I_{003}/I_{104} for all the oxides are above 1.85, indicating scarcely any confusion of Li$^+$ and Ni^{+2}.

SEM images of Li[Li$_{0.2}$Mn$_{0.54}$Ni$_{0.13}$Co$_{0.13}$]O$_2$, Li[Li$_{0.2}$Mn$_{0.54}$Ni$_{0.13}$Co$_{0.13}$]O$_2$/LiCl and Li[Li$_{0.2}$Mn$_{0.54}$Ni$_{0.13}$Co$_{0.13}$]O$_2$/KCl are shown in Fig. 2. The morphologies of the layered oxide particles treated in air, LiCl and KCl molten salts are much different. The bare Li[Li$_{0.2}$Mn$_{0.54}$Ni$_{0.13}$Co$_{0.13}$]O$_2$ calcined in air has ball-like primary particles with sizes of 50–150 nm. It seems that the alkali chloride molten salts significantly affect the particle growth of the layered oxide, leading to the morphology change. The particles of Li
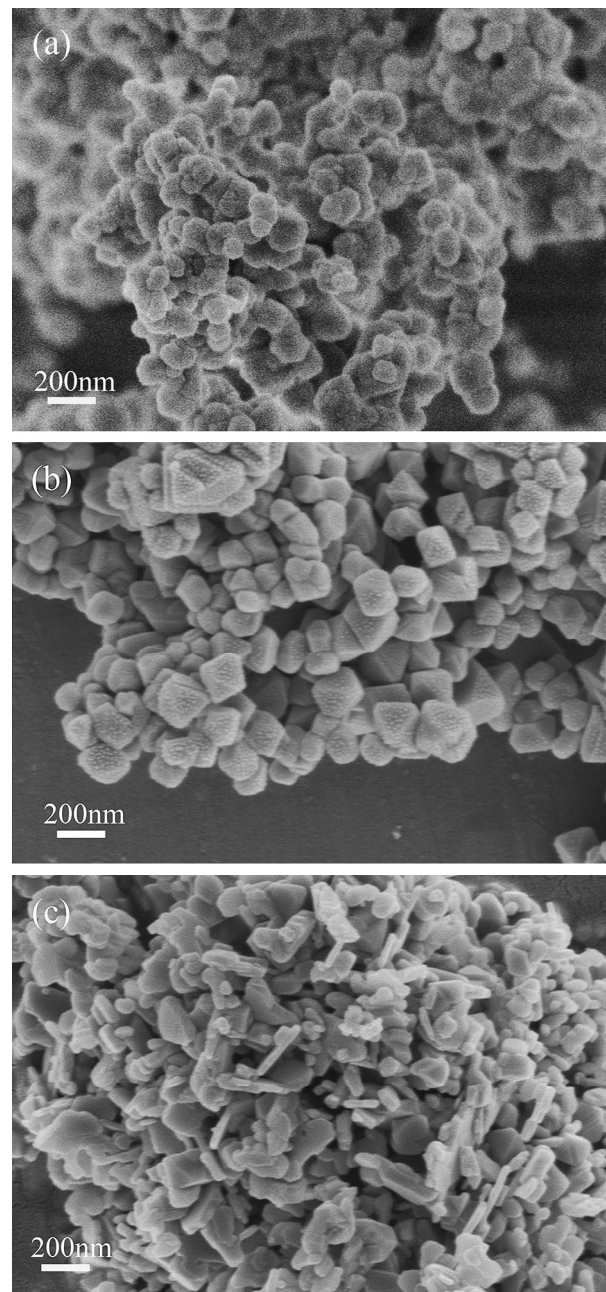
[Li$_{0.2}$Mn$_{0.54}$Ni$_{0.13}$Co$_{0.13}$]O$_2$/LiCl become cube-like with specific surface area reduced from 7.817 m^2 g^{-1} for the bare Li[Li$_{0.2}$Mn$_{0.54}$Ni$_{0.13}$Co$_{0.13}$]O$_2$ to 6.573 m^2 g^{-1}. And the particle sizes obtained from the SEM image are 200–300 nm. The morphology of Li[Li$_{0.2}$Mn$_{0.54}$Ni$_{0.13}$Co$_{0.13}$]O$_2$/KCl also changes a lot. Plate-like particles with thicknesses of 20–30 nm are obtained when the layered oxide is treated in KCl molten salt. The specific surface area of Li[Li$_{0.2}$Mn$_{0.54}$Ni$_{0.13}$Co$_{0.13}$]O$_2$/KCl has a remarkable increase, 17.05 m^2 g^{-1}, twice more than that of the bare one. It is speculated that during the heat treatment in KCl, the K ions may cover the surface of the oxide due to the electrostatic interaction to block one aspect of the particle growth, resulting in plate-like morphology.

Fig. 3 shows the TEM images of Li[Li$_{0.2}$Mn$_{0.54}$Ni$_{0.13}$Co$_{0.13}$]O$_2$ synthesized with or without alkali chloride molten salts. The oxide
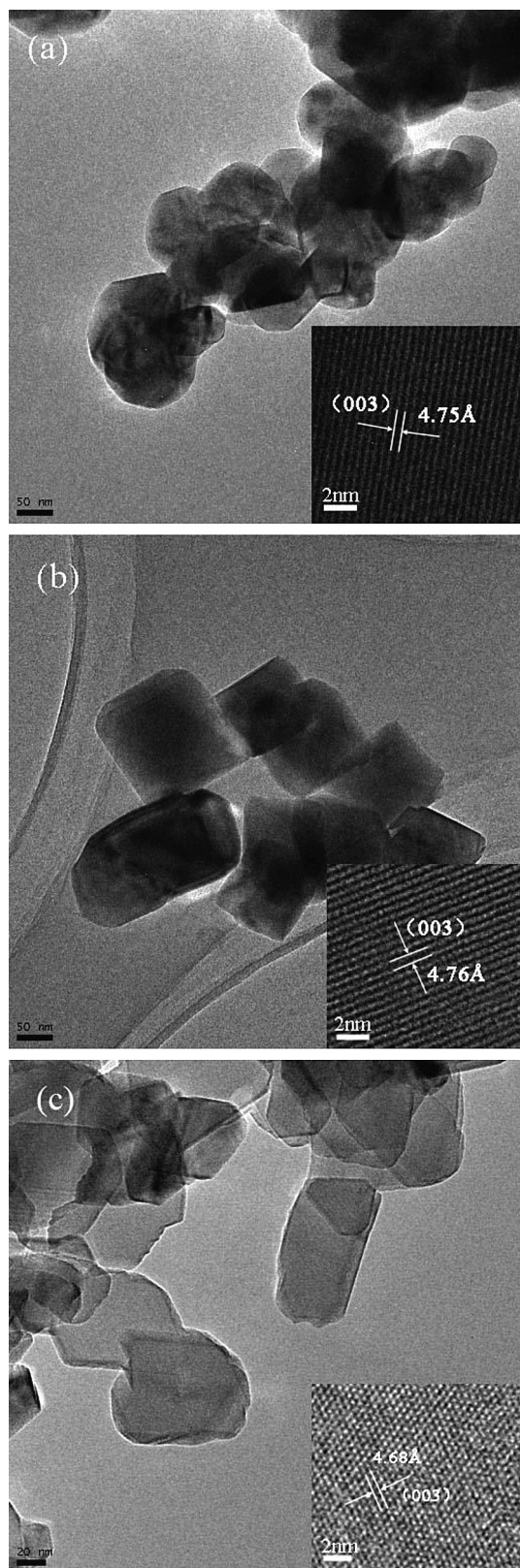
Fig. 3. TEM images of Li[Li$_{0.2}$Mn$_{0.54}$Ni$_{0.13}$Co$_{0.13}$]O$_2$ powders: (a) calcined in air, (b) treated in LiCl molten salt and (c) treated in KCl molten salt.

particles of bare Li[Li$_{0.2}$Mn$_{0.54}$Ni$_{0.13}$Co$_{0.13}$]O$_2$ are 100–150 nm in sizes (Fig. 3(a)). For Li[Li$_{0.2}$Mn$_{0.54}$Ni$_{0.13}$Co$_{0.13}$]O$_2$/LiCl, cube-like particles are 200–300 nm in sizes. Thin plate-like particles are observed as the oxide is dipped in KCl molten salt during high

temperature calcination. The HRTEM image shows that all the oxide particles have perfect crystallinity with distinct lattice fringes (the insert in Fig. 3(a)–(c)). The distance between the neighboring lattice fringes has an approximate d-spacing value of 4.7 Å, which corresponds to the (003) plane of the hexagonal layered phase.

The surface composition and oxidation state of the elements were analyzed by XPS. Fig. 4 shows the XPS spectra of Li[Li$_{0.2}$Mn$_{0.54}$Ni$_{0.13}$Co$_{0.13}$]O$_2$, Li[Li$_{0.2}$Mn$_{0.54}$Ni$_{0.13}$Co$_{0.13}$]O$_2$/LiCl and Li[Li$_{0.2}$Mn$_{0.54}$Ni$_{0.13}$Co$_{0.13}$]O$_2$/KCl. The dashed lines indicate that after the treatment in the molten salts, Co^{3+}, Mn^{4+} and Ni^{2+} 2P$_{3/2}$ remain at their original binding energies of 780.1, 642.6 and 854.9 eV, respectively [41]. For the Mn element, the binding energy of Mn^{3+} should be around 641.3 eV (Mn$_2$O$_3$) and that of Mn^{4+} should be around 642.1 eV (MnO$_2$). Therefore, the valences of Mn, Co, Ni do not change after the treatment in molten salts, indicating that the Co, Ni, and Mn ion environments in the structure are not changed. It is concluded that the heat-treatment process in molten salts does not charge the chemical environment of the active material. The surface O^{2-} ions are not substituted by Cl$^-$.

3.2. Electrochemical properties

Fig. 5 shows the initial charge–discharge curves of Li[Li$_{0.2}$Mn$_{0.54}$Ni$_{0.13}$Co$_{0.13}$]O$_2$ electrodes at a current density of 20 mA g^{-1} in the voltage range of 2.0–4.8 V. As normal Li-rich layered oxides, there are two charge platforms for the initial cycle, one at 4.0 V and the other at about 4.5 V. The first one at about 4.0 V is the Li-extraction from the structure of space group R-3m accompanying with the oxidation of mainly Ni^{2+}/Ni^{4+}. The other at 4.5 V represents the activation of the Li$_2$MnO$_3$-like region which is irreversible and appears only in the initial cycle. During the initial charge process, Li$^+$ in the Li$_2$MnO$_3$-like region will be extracted at about 4.5 V accompanying with loss of O. Then the electrochemical inactive Li$_2$MnO$_3$ region became active after removing of Li$_2$O from the lattice and forming [MnO$_2$] [42]. The achievement of the activation process will significantly increase the amount of Li-reinsertion, resulting in high discharge capacity for the following cycles. The bare Li[Li$_{0.2}$Mn$_{0.54}$Ni$_{0.13}$Co$_{0.13}$]O$_2$ has large initial charge and discharge capacities of 364.2 and 290.1 mAh g^{-1}, respectively. Its charge capacity approaches to the theoretical value (377.1 mAh g^{-1}, calculated from the parent Li[Li$_{0.2}$Mn$_{0.54}$Ni$_{0.13}$Co$_{0.13}$]O$_2$). However, the initial coulombic efficiency is low, only about 79.7%, large capacity is lost during the initial cycle. The lost capacity is ascribed to the irreversible removal of Li$_2$O from the Li$_2$MnO$_3$ region, and the formation of SEI film. The removal of Li$_2$O from the Li$_2$MnO$_3$ region is the main reason for the low initial coulombic efficiency due to its irreversibility [42,43]. Furthermore, the initial discharge capacity surpasses the theoretic value (276 mAh g^{-1}, calculated from LiMO$_2$, M = Mn, Co, Ni, after activation). It is reported that anomalously high capacity above the theoretically expected value can be obtained from Li[Li$_{0.2}$Mn$_{0.54}$Ni$_{0.13}$Co$_{0.13}$]O$_2$ [43,44]. Although the origin of the exceptionally high capacity is not yet known, it has been speculated that the anomalous capacity is due to oxygen ion vacancies, which are attributed to the removal of Li$_2$O during the first cycle activation. The as-produced oxygen ion vacancies which were partly maintained temporarily could accommodate the Li$^+$ during the following discharge process, leading to the anomalous capacity for the initial cycle [43,44]. As we can see, Li[Li$_{0.2}$Mn$_{0.54}$Ni$_{0.13}$Co$_{0.13}$]O$_2$/LiCl also has high charge and discharge capacities of 348.2 and 277.2 mAh g^{-1} at a current density of 20 mA g^{-1}, respectively, a little lower than those of the bare one. And Li[Li$_{0.2}$Mn$_{0.54}$Ni$_{0.13}$Co$_{0.13}$]O$_2$/KCl exhibits a high initial discharge capacity of 299.2 mAh g^{-1} as well as an initial charge capacity of 356.4 mAh g^{-1}.

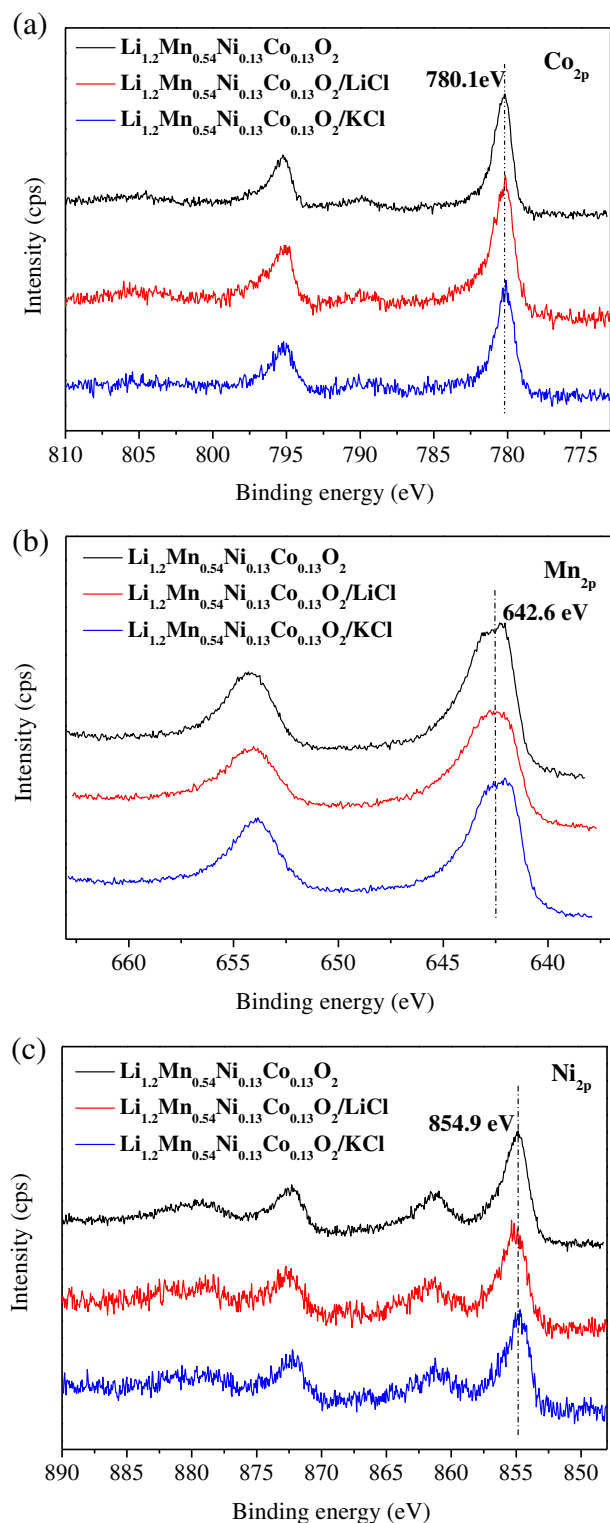**Fig. 4.** XPS spectra of Li[Li$_{0.2}$Mn$_{0.54}$Ni$_{0.13}$Co$_{0.13}$]O$_2$ with or without molten salt treatment.

Fig. 5. Charge−discharge curves of Li[Li$_{0.2}$Mn$_{0.54}$Ni$_{0.13}$Co$_{0.13}$]O$_2$ electrodes at a current density of 20 mA g^{-1}.

[Li$_{0.2}$Mn$_{0.54}$Ni$_{0.13}$Co$_{0.13}$]O$_2$/KCl. It seems that the treatment in KCl molten salt significantly increases the specific surface area of the layered oxide, leading to more formation of SEI film, shorter Li$^+$ diffusion distance, more thorough activation in the initial charge. Thus, even at a current density of 200 mA g^{-1}, a high discharge capacity approaching to theoretic value can be obtained. However, the activation process of the layered oxide after treated in LiCl molten salt is slowed up according to the analysis of XRD patterns, leading to a low initial discharge of 157.1 mAh g^{-1}. It can also be observed in the cycling tests at a current density of 200 mA g^{-1} later and the capacity contribution in the activation section for the initial charge. The capacity of the activation part for the bare Li [Li$_{0.2}$Mn$_{0.54}$Ni$_{0.13}$Co$_{0.13}$]O$_2$ is about 210 mAh g^{-1} at a current density of 200 mA g^{-1} as shown in Fig. 4, about 67.7% of the total capacity of both platforms at 3.9 V and 4.5 V, which is accordant with the theoretical value (66.7%, calculated from 0.6Li[Li$_{1/3}$Mn$_{2/3}$]O$_2$·0.4Li [Mn$_{1/3}$Ni$_{1/3}$Co$_{1/3}$]O$_2$). The similar results are also obtained for both Li[Li$_{0.2}$Mn$_{0.54}$Ni$_{0.13}$Co$_{0.13}$]O$_2$/LiCl and Li[Li$_{0.2}$Mn$_{0.54}$Ni$_{0.13}$Co$_{0.13}$]O$_2$/ KCl. However, at a current density of 200 mA g^{-1}, the capacity contribution of the activation section decreases, about 61.4% and 63.3% for bare Li[Li$_{0.2}$Mn$_{0.54}$Ni$_{0.13}$Co$_{0.13}$]O$_2$ and Li[Li$_{0.2}$Mn$_{0.54}$Ni$_{0.13}$Co$_{0.13}$]O$_2$/KCl, respectively. Li[Li$_{0.2}$Mn$_{0.54}$Ni$_{0.13}$Co$_{0.13}$]O$_2$/LiCl has the least capacity contribution of only about 47.4%, implying that the activation of the Li$_2$MnO$_3$-like region is the most difficult for the oxide after treated in LiCl molten salt. Furthermore, since the proportion of the activation charge capacity in total capacity is much smaller than the theoretical value at high current density, it indicates that the activation of the Li$_2$MnO$_3$-like region is not thoroughly performed at the initial cycle. Thus, a long activation process can be observed from the cycle tests later in Fig. 6(b). And if we first cycle the cell at a current density of 20 mA g^{-1} for a cycle as shown in Fig. 6(b), the following discharge capacity immediately increases to 197.9 mAh g^{-1}, and the long activation process disappears. It seems that such cube-like particle with specific crystal facet may be adverse for the activation process, especially at high current density. The mechanism of the activation is very complex and needs further investigation.

Fig. 6(b) shows the cycle performances of Li[Li$_{0.2}$Mn$_{0.54}$Ni$_{0.13}$Co$_{0.13}$]O$_2$ electrodes at a current density of 200 mA g^{-1} in the voltage of 2.0−4.8 V. The bare Li[Li$_{0.2}$Mn$_{0.54}$Ni$_{0.13}$Co$_{0.13}$]O$_2$ has the highest discharge capacity of 243.1 mAh g^{-1} with capacity retention of 71.2% after 80 cycles. Li[Li$_{0.2}$Mn$_{0.54}$Ni$_{0.13}$Co$_{0.13}$]O$_2$/KCl which has the highest discharge capacity of 254.1 mAh g^{-1} among all the oxides exhibits the poorest cycle stability with capacity retention of

Fig. 6(a) shows the initial charge−discharge capacities of the oxide electrodes at a current density of 200 mA g^{-1}. The initial charge process can also be divided into two parts, just the same as that at 20 mA g^{-1}. The bare Li[Li$_{0.2}$Mn$_{0.54}$Ni$_{0.13}$Co$_{0.13}$]O$_2$ delivers a high initial discharge capacity of 236.6 mAh g^{-1} at 200 mA g^{-1}, and remarkable discharge capacity of 253.6 mAh g^{-1} is obtained for Li
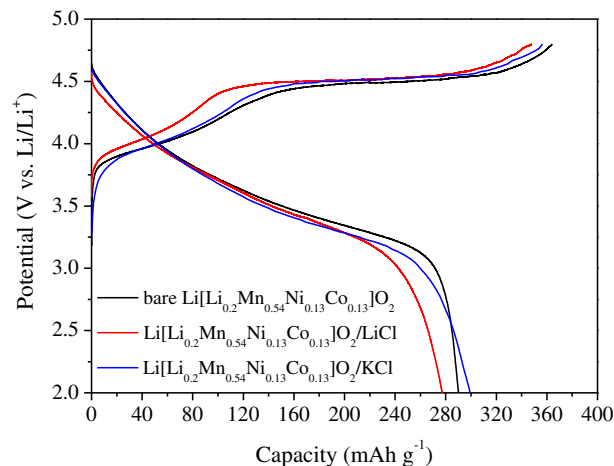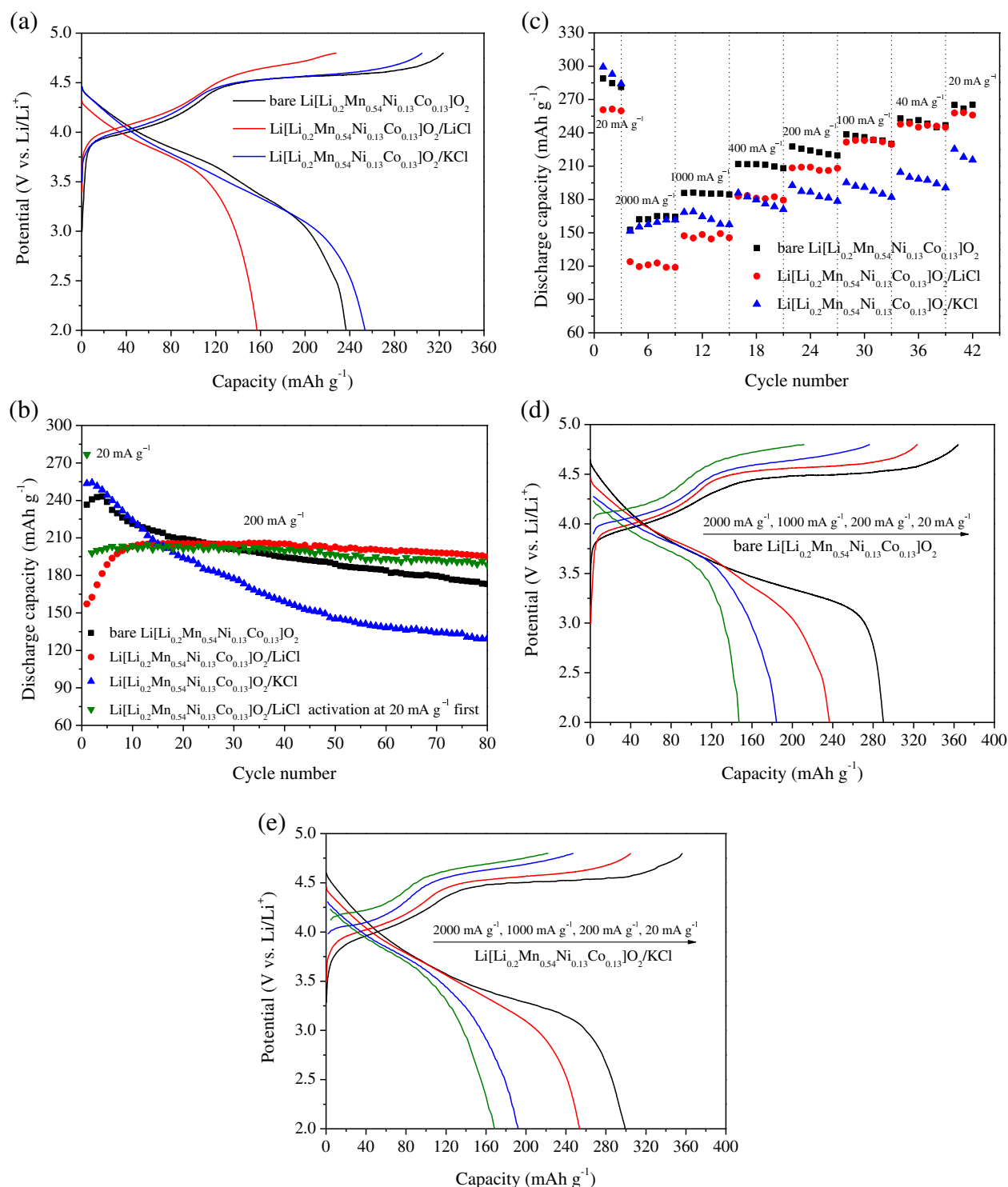
Fig. 6. (a) Initial charge–discharge curves, (b) cycle performance of Li[Li$_{0.2}$Mn$_{0.54}$Ni$_{0.13}$Co$_{0.13}$]O$_2$ at a current density of 200 mA g^{-1}, (c) rate capability of Li[Li$_{0.2}$Mn$_{0.54}$Ni$_{0.13}$Co$_{0.13}$]O$_2$ at different current densities, (d) initial charge–discharge curves of Li[Li$_{0.2}$Mn$_{0.54}$Ni$_{0.13}$Co$_{0.13}$]O$_2$ and (e) Li[Li$_{0.2}$Mn$_{0.54}$Ni$_{0.13}$Co$_{0.13}$]O$_2$/KCl at different current densities.

only 51.0% after 80 cycles. However, improved cycle stability is obtained for Li[Li$_{0.2}$Mn$_{0.54}$Ni$_{0.13}$Co$_{0.13}$]O$_2$/LiCl with capacity retention of 94.9% after 80 cycles. Two main factors have been demonstrated to affect the cycle stability [45–48]. One is the dissolution of the transition metal ions, especially the manganese ion during charge–discharge process. The mechanism of the Mn dissolution can be explained as follows:

$$Mn^{3+} \xrightarrow{charge-discharge} Mn^{4+} + Mn^{2+} \tag{1}$$
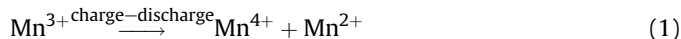
Part of Mn^{4+} will be reduced to Mn^{3+} especially when the cells are discharged to a low potential of 2.0 V. This part of the Mn element will easily dissolve. The dissolution will seriously destroy the oxide surface and unsatisfactory SEI film will form [13,17]. The other is the Jahn–Teller distortion during the cycling process. If Li

$[Li_{0.2}Mn_{0.54}Ni_{0.13}Co_{0.13}]O_2$ completely delithiated during charge, then it would yield $Mn_{0.675}Ni_{0.1625}Co_{0.1625}O_2$ (Only when Li extracted form Li_2MnO_3, there are O lost.) in which the manganese ions were tetravalent [42]. Thus, $Li[Li_{0.2}Mn_{0.54}Ni_{0.13}Co_{0.13}]O_2/KCl$ which has large specific surface area has serious side-reactions with the electrolyte during charge and discharge process, resulting in rapid decrease of discharge capacity [17,49]. For Li $[Li_{0.2}Mn_{0.54}Ni_{0.13}Co_{0.13}]O_2/LiCl$, a high capacity retention is obtained with a little capacity sacrifice due to the lowest specific surface area which reduces the dissolution of the transition metal ions [13].

Rate capability of $Li[Li_{0.2}Mn_{0.54}Ni_{0.13}Co_{0.13}]O_2$ is displayed in Fig. 6(c) from current density of 20—2000 mA g^{-1} between 2.0 V and 4.8 V. The cells were charged and discharged at the same current density. The bare $Li[Li_{0.2}Mn_{0.54}Ni_{0.13}Co_{0.13}]O_2$ delivers discharge capacities of 290.1, 253.0, 238.6, 227.7, 211.9, 186.1 and 165.0 mAh g^{-1} at current densities 20, 40, 100, 200, 400, 1000 and 2000 mA g^{-1}, respectively. However, the initial discharge capacity of $Li[Li_{0.2}Mn_{0.54}Ni_{0.13}Co_{0.13}]O_2/KCl$ is higher than that of the bare one. Due to the plate-like nanoparticles with large specific surface area, the discharge capacity of $Li[Li_{0.2}Mn_{0.54}Ni_{0.13}Co_{0.13}]O_2/KCl$ becomes the worst in the following tests except for that at a current density of 2000 mA g^{-1}. In order to exhibit the excellent rate capability of $Li[Li_{0.2}Mn_{0.54}Ni_{0.13}Co_{0.13}]O_2/KCl$ without the influence of capacity attenuation, initial charge—discharge curves at different current densities for bare $Li[Li_{0.2}Mn_{0.54}Ni_{0.13}Co_{0.13}]O_2$ and Li $[Li_{0.2}Mn_{0.54}Ni_{0.13}Co_{0.13}]O_2/KCl$ are shown in Fig. 6(d) and (e). Li $[Li_{0.2}Mn_{0.54}Ni_{0.13}Co_{0.13}]O_2/KCl$ delivers discharge capacities of 192.3 mAh g^{-1} and 168.5 mAh g^{-1} at current densities of 1000 mA g^{-1} and 2000 mA g^{-1}, respectively, higher than the bare one (184.2 mAh g^{-1} and 147.3 mAh g^{-1} for comparison). From all the above, the molten salt treatment can not only control the particle morphology, but also reform the electrochemical performances of the Li-rich layered oxide for various applications.

Fig. 7 shows the CV curves of the Li-rich layered oxides for the initial three cycles. All the electrodes have similar shapes of the CV curves, indicating no intrinsic change after treated in different molten salts. The initial CV curve for the oxidation section is sharp, symmetrical and accordant with the initial charge curve. There are two main anodic peaks, one at about 3.9 V and another at about 4.6 V (vs. Li/Li$^+$). The one at 3.9 V is ascribed to the extraction of Li$^+$ from the $LiMO_2$ (M = Mn, Ni, Co) structure. And the other at 4.6 V corresponds to the activation of the Li_2MnO_3 region, extraction of Li$^+$ from $Li[Li_{1/3}Mn_{2/3}]O_2$ [43]. However, the activation peak disappears at the second cycle and a broad peak appears at 3.85 V which is the main anodic peak for the newly formed oxide, containing the oxidation of Ni and Co element. The other anode peak at about 4.5 V at the second cycle is due to the partial redox contribution from Co^{3+} to Co^{4+} that corresponds to the second electron transfer in Li-rich layered oxide [50]. In addition, it seems that the anodic peak appears at about 3.2 V is more evident for Li $[Li_{0.2}Mn_{0.54}Ni_{0.13}Co_{0.13}]O_2/KCl$. The anode peak at 3.8 V is a broad peak which may contain many reactions, thus there should also be a peak at around 3.2 V for bare $Li[Li_{0.2}Mn_{0.54}Ni_{0.13}Co_{0.13}]O_2$ and Li $[Li_{0.2}Mn_{0.54}Ni_{0.13}Co_{0.13}]O_2/LiCl$. For $Li[Li_{0.2}Mn_{0.54}Ni_{0.13}Co_{0.13}]O_2/KCl$, however, the peak may move to the low potential for some reason such as large surface area, small scale at one aspect and so on. The other probability is due to the repeated washing for the KCl treated sample. As we state in the ICP-AES test, there are a few Li ions lost. Although such amount of Li lost will not change the layered structure, but the new formed $[MO_2]$ may be a little different. The process of the oxidation is also very complicated for such Li-rich oxide and further woke is necessary to make it clear.

Two cathodic peaks are evident during the discharge process. The reduction processes is too complex and is impossible to differentiate [51]. From Fig. 7(a)—(c), it clearly reveals that after
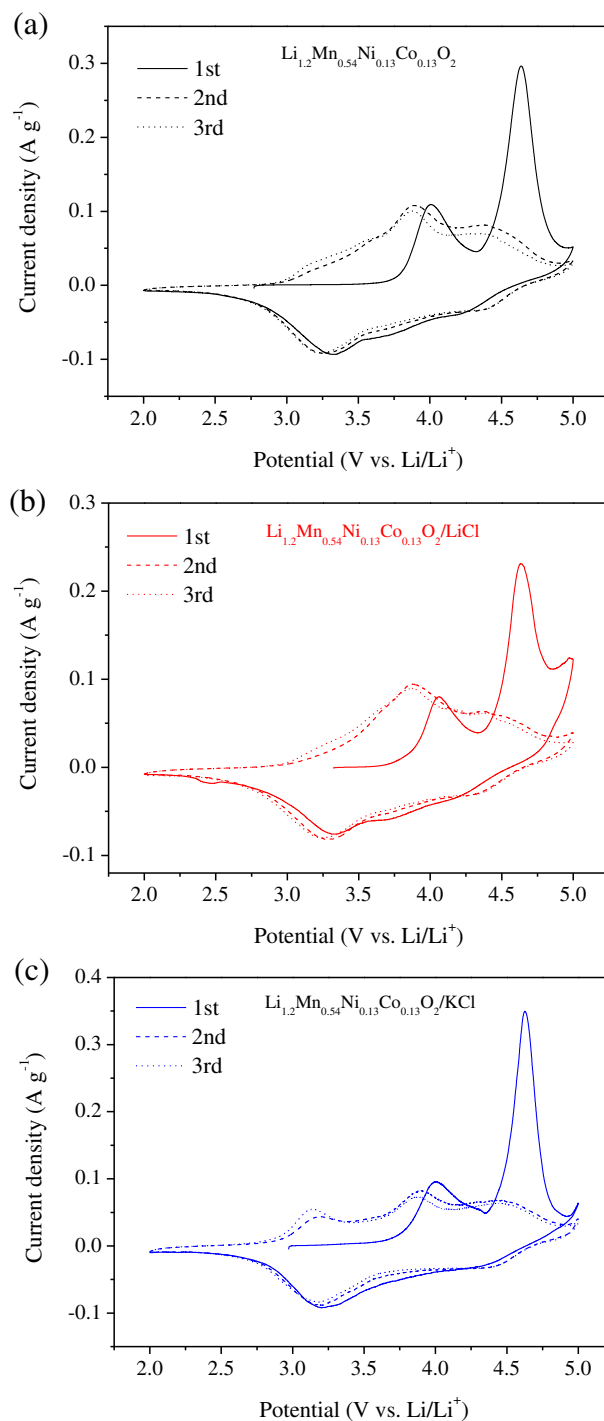

(a)

(b)

(c)

Fig. 7. CV curves of $Li[Li_{0.2}Mn_{0.54}Ni_{0.13}Co_{0.13}]O_2$ electrodes for the initial three cycles (scan rate: 0.1 mV s^{-1}, potential range: 2.0—5.0 V).

treated in LiCl molten salt, the initial activation process is reduced as the intensity of the peak at 4.6 V is much lower than the bare one. It indicates that the activation of the oxide becomes difficult after treated in LiCl molten salt. However, for the oxide treated in KCl molten salt, the phenomenon is different. The peak at 4.6 V becomes more symmetrical and sharper, indicating easier activation due to the plate-like nanoparticle obtained. In addition, due to the prolonged activation processes for $Li[Li_{0.2}Mn_{0.54}Ni_{0.13}Co_{0.13}]O_2/LiCl$, the intensity of cathodic peaks for the second and third cycles is much higher than that of the initial one, indicating that more active
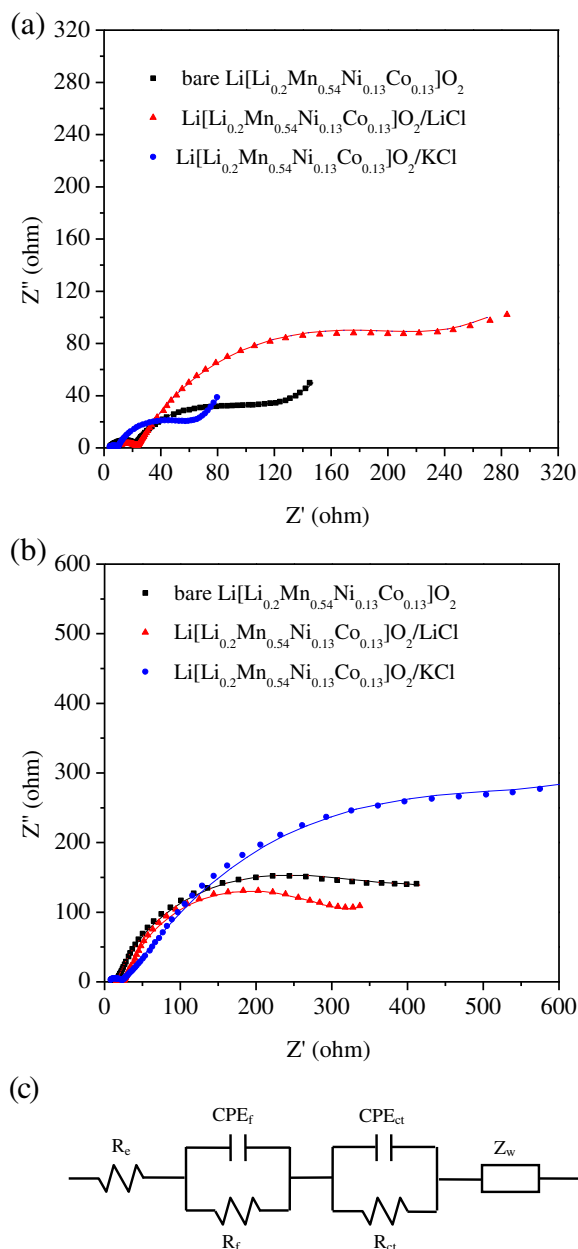
Fig. 8. Nyquist plots of Li[Li$_{0.2}$Mn$_{0.54}$Ni$_{0.13}$Co$_{0.13}$]O$_2$ electrodes after (a) 1 cycle and (b) 50 cycles at the charge state of 4.5 V, the real lines in (a) and (b) are the fitting results of the Nyquist plots with the equivalent circuit (c) equivalent circuit to fit the curves in (a) and (b).

[MO$_2$] appear after the second and third oxidation processes. Contrarily, only for Li[Li$_{0.2}$Mn$_{0.54}$Ni$_{0.13}$Co$_{0.13}$]O$_2$/KCl with plate-like morphology, the intensity of cathodic peaks for the second and third cycles is distinctly lower than that of the initial one. It is ascribed to the thorough activation in the initial oxidation process.

EIS tests were performed to further understand the effect of the molten salt treatment on the layered oxide. The cells were cycled at a current density of 200 mA g^{-1} for 1 cycle and 50 cycles and then charged to 4.5 V at a current density of 20 mA g^{-1}. Fig. 8(a) and (b) shows the Nyquist plots of Li-rich layered oxide electrodes. The shapes of all the Nyquist plots are similar. They are composed of a small interrupt and a semicircle in the high frequency, a semicircle in the high to medium frequency and a quasi-straight line in the low frequency. The small interrupt in the high frequency which

corresponds to the solution impedance R_e, is almost the same for all the electrodes. The small semicircle in the high frequency is assigned to the impedance (R_f) of Li$^+$ diffusion in the surface layer (SEI film); another semicircle in the high to medium frequency indicates the charge transfer impedance (R_{ct}), relating to charge transfer through the electrode/electrolyte interface. And the quasi-straight line in the low frequency represents the Warburg impedance, which is related to the solid-state diffusion of Li$^+$ in the electrode [21,52]. In order to further understand the Nyquist plots, an equivalent circuit is used to fit them, as shown in Fig. 8(c) and the results of the fitting are also shown in Fig. 8(a) and (b) (the real line in the figures). CEP$_f$, CEP$_{ct}$ and Z_w represent the non-ideal capacitance of the surface layer, non-ideal capacitance of the double-layer and Warburg impedance, respectively. As shown in Table 1, the values of R_f and R_{ct} of Li[Li$_{0.2}$Mn$_{0.54}$Ni$_{0.13}$Co$_{0.13}$]O$_2$/KCl are rather small at the beginning, 6.17 Ω and 38.4 Ω, respectively, resulting from the large specific surface area and thorough activation. However, Li[Li$_{0.2}$Mn$_{0.54}$Ni$_{0.13}$Co$_{0.13}$]O$_2$/LiCl exhibits large values of R_f and R_{ct}, 13.97 Ω and 181.6 Ω, respectively. It seems that the activation will improve the electrochemical performance of the material with reduction of R_f and R_{ct} due to the intrinsic change of [MO$_2$] formation, but disorder the lattice and destroy the surface structure due to the extraction of O. Thus, the oxide surface becomes weak and is easily corroded by the electrolyte during the charge–discharge process, especially for Li[Li$_{0.2}$Mn$_{0.54}$Ni$_{0.13}$Co$_{0.13}$]O$_2$/KCl with much larger specific surface area.

It clearly reveals that after 50 cycles, the values of R_f and R_{ct} increase a lot, 20.16 Ω and 601.3 Ω are obtained for Li[Li$_{0.2}$Mn$_{0.54}$Ni$_{0.13}$Co$_{0.13}$]O$_2$/KCl. On one side, the transition metal ions dissolve in the electrolyte from the weak surface. The as-dissolved metal ions will deposit back on the surface and then a thick SEI film with poor conduction of electron and Li$^+$ will form, leading to increase in R_f and R_{ct} [13]. Thus, the capacity of Li[Li$_{0.2}$Mn$_{0.54}$Ni$_{0.13}$Co$_{0.13}$]O$_2$/KCl decreases rapidly. R_f and R_{ct} of Li[Li$_{0.2}$Mn$_{0.54}$Ni$_{0.13}$Co$_{0.13}$]O$_2$/LiCl can be maintained at low values of 10.15 Ω and 245.4 Ω, respectively, resulting in a more stable cycle. In addition, the bare Li[Li$_{0.2}$Mn$_{0.54}$Ni$_{0.13}$Co$_{0.13}$]O$_2$ has a moderate change of R_f and R_{ct} between Li[Li$_{0.2}$Mn$_{0.54}$Ni$_{0.13}$Co$_{0.13}$]O$_2$/KCl and Li[Li$_{0.2}$Mn$_{0.54}$Ni$_{0.13}$Co$_{0.13}$]O$_2$/LiCl, which are also accordant with the electrochemical performances.

GITT tests were carried out to evaluate Li$^+$ diffusion in the Li-rich layered oxide. The processes of the calculation of the D_{Li^+} have been reported in our previous work [27]. And the values of D_{Li^+} during the initial charge–discharge have been shown in Fig. 9(a) and (b). The results of the charge sections have a similar rule to the initial charge curve shown in Fig. 4. At the charge process from 3.8 to 4.2 V, the Li$^+$ probably extracts from the R-3m structure LiMO$_2$ (M = Mn, Ni, Co) region. And D_{Li^+} approaches to a constant value. However, D_{Li^+} decreases rapidly as the charge process is proceeding, and a minimum D_{Li^+} is obtained at the end of the first charge platform of about 4.50 V. As the charge process goes along, the D_{Li^+} increases again, corresponding to the activation section of the Li$_2$MnO$_3$ region. It indicates that the Li$^+$ diffusion in the Li$_2$MnO$_3$ region is slower than that in the LiMO$_2$ (M = Mn, Ni, Co) region. In

Table 1
The values of R_f and R_{ct} for the EIS fitting after 1 cycle and 50 cycles.

Samples	After 1 cycle		After 50 cycles	
	R_f (Ω)	R_{ct} (Ω)	R_f (Ω)	R_{ct} (Ω)
Bare Li[Li$_{0.2}$Mn$_{0.54}$Ni$_{0.13}$Co$_{0.13}$]O$_2$	19.88	80.12	7.33	332.7
Li[Li$_{0.2}$Mn$_{0.54}$Ni$_{0.13}$Co$_{0.13}$]O$_2$/LiCl	13.97	181.6	10.15	245.4
Li[Li$_{0.2}$Mn$_{0.54}$Ni$_{0.13}$Co$_{0.13}$]O$_2$/KCl	6.17	38.4	20.16	601.3

(a)

(b)
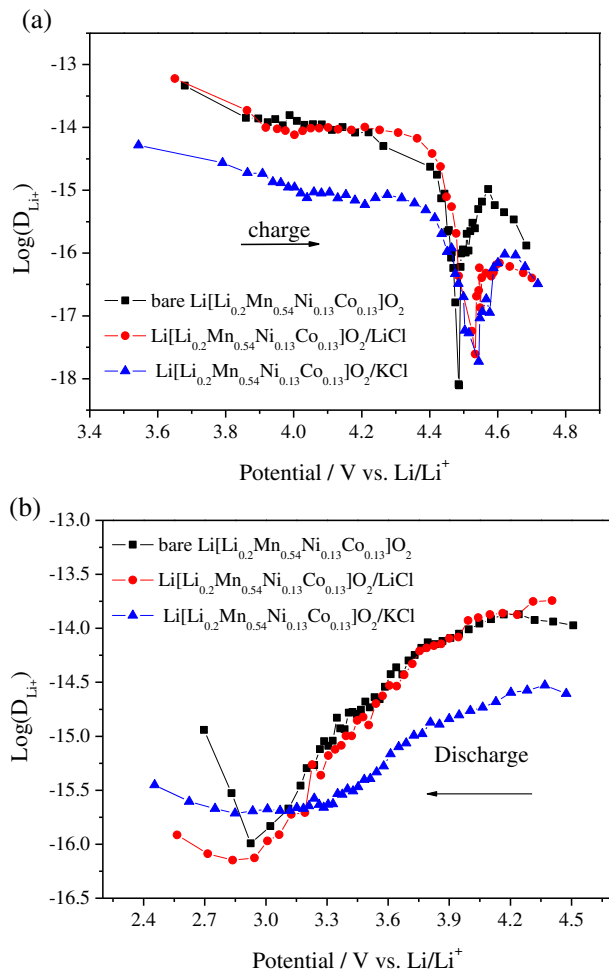
Fig. 9. Diffusion coefficients of Li$^+$ in Li[Li$_{0.2}$Mn$_{0.54}$Ni$_{0.13}$Co$_{0.13}$]O$_2$ determined by GITT: (a) at charge states, (b) at discharge states.

comparison with the bare Li[Li$_{0.2}$Mn$_{0.54}$Ni$_{0.13}$Co$_{0.13}$]O$_2$, the D_{Li^+} of Li[Li$_{0.2}$Mn$_{0.54}$Ni$_{0.13}$Co$_{0.13}$]O$_2$/KCl becomes a little small during the whole charge process. For Li[Li$_{0.2}$Mn$_{0.54}$Ni$_{0.13}$Co$_{0.13}$]O$_2$/LiCl, however, only the D_{Li^+} of the activation section becomes a little small. Fig. 9(b) shows the variation of D_{Li^+} during the whole discharge process. It decreases almost during the whole discharge process from 4.2 V to 2.9 V.

Furthermore, the reactions during the charge–discharge process are extremely complex, which include not only Li$^+$ diffusion but also oxygen loss, metal ion dissolution and structural rearrangement. Thus, the D_{Li^+} obtained here should be regarded as pseudo or apparent diffusion coefficients [53]. To compare with typical layered oxides such as LiCoO$_2$ (10^{-7}–10^{-11} cm^2 s^{-1}) [54] and LiNi$_{1/3}$Co$_{1/3}$Mn$_{1/3}$O$_2$ (10^{-9}–10^{-10} cm^2 s^{-1}) [55], the D_{Li^+} obtained is extremely small. This is understandable because abundant lattice disorders are produced during the transformation from Li[Li$_{0.2}$Mn$_{0.54}$Ni$_{0.13}$Co$_{0.13}$]O$_2$ to Li$_x$MO$_2$. The resultant crystal lattice is not perfect, which therefore retards the Li$^+$ diffusion. The excellent rate capability of Li[Li$_{0.2}$Mn$_{0.54}$Ni$_{0.13}$Co$_{0.13}$]O$_2$/KCl in this work is attributed to the plate-like particles with thicknesses of 20–30 nm, which significantly enlarges the interface between the oxide and electrolyte, shortens the diffusion distance of Li$^+$ and is independent of the D_{Li^+}. Furthermore, it seems that the low discharge capacity obtained for Li[Li$_{0.2}$Mn$_{0.54}$Ni$_{0.13}$Co$_{0.13}$]O$_2$/LiCl is also independent of D_{Li^+}.

4. Conclusions

Cube-like and plate-like Li[Li$_{0.2}$Mn$_{0.54}$Ni$_{0.13}$Co$_{0.13}$]O$_2$ particles with well-formed layered structure and high crystallinity are obtained after treated in LiCl and KCl molten salts, respectively. Furthermore, improved rate capability is obtained after treated in KCl molten salt, while enhanced cycle stability is obtained after treated in LiCl molten salt. EIS and GITT show that such electrochemical performance change is attributed to their morphology and specific surface area, but is independent of Li$^+$ diffusion coefficient. It appears that the treatment in molten salt can effectively reform the electrochemical performances of the Li[Li$_{0.2}$Mn$_{0.54}$Ni$_{0.13}$Co$_{0.13}$]O$_2$ cathode material for various practical application.

Acknowledgments

References

[1] J. Gao, J. Kim, A. Manthiram, Electrochem. Commun. 11 (2009) 84.
[2] S.J. Shi, J.P. Tu, Y.Y. Tang, Y.X. Yu, Y.Q. Zhang, X.L. Wang, J. Power Sources 221 (2013) 300.
[3] J.H. Lim, H. Bang, K.S. Lee, K. Amine, Y.K. Sun, J. Power Sources 189 (2009) 571.
[4] S.H. Kang, M.M. Thackeray, Electrochem. Commun. 11 (2009) 748.
[5] J.Y. Xiang, J.P. Tu, L. Zhang, X.L. Wang, Y. Zhou, Y.Q. Qiao, Y. Lu, J. Power Sources 195 (2010) 8331.
[6] S.J. Shi, J.P. Tu, Y.Y. Tang, X.Y. Liu, Y.Q. Zhang, X.L. Wang, C.D. Gu, Electrochim. Acta 88 (2013) 671.
[7] Y.J. Wei, K. Nikolowski, S.Y. Zhan, H. Ehrenberg, S. Oswald, G. Chen, C.Z. Wang, H. Chen, Electrochem. Commun. 11 (2009) 2008.
[8] W.L. Liu, J.P. Tu, Y.Q. Qiao, J.P. Zhou, S.J. Shi, X.L. Wang, C.D. Gu, J. Power Sources 196 (2011) 7728.
[9] J. Wang, G.X. Yuan, M.B. Zhang, B. Qiu, Y.G. Xia, Z.P. Liu, Electrochim. Acta 66 (2012) 61.
[10] C.J. Jafta, K.I. Ozoemena, M.K. Mathe, W.D. Roos, Electrochim. Acta 85 (2012) 411.
[11] W.C. West, J. Soler, B.V. Ratnakumar, J. Power Sources 204 (2012) 200.
[12] J.H. Kim, M.S. Park, J.H. Song, D.J. Byun, Y.J. Kim, J.S. Kim, J. Alloys Compd. 517 (2012) 20.
[13] J.M. Zheng, X.B. Wu, Y. Yang, Electrochim. Acta 56 (2011) 3071.
[14] S. Kim, C. Kim, Y.-I. Jhon, J.-K. Noh, S.H. Vemuri, R. Smith, K.Y. Chung, M.S. Jhon, B.-W. Cho, J. Mater. Chem. 22 (2012) 25418.
[15] S.J. Shi, J.P. Tu, Y.J. Mai, Y.Q. Zhang, C.D. Gu, X.L. Wang, Electrochim. Acta 63 (2012) 112.
[16] J.M. Zheng, Z.R. Zhang, X.B. Wu, Z.X. Dong, Z. Zhu, Y. Yang, J. Electrochem. Soc. 155 (2008) A775.
[17] D.Y.W. Yu, K. Yanagida, H. Nakamura, J. Electrochem. Soc. 157 (2010) A1177.
[18] C.S. Johnson, N. Li, C. Lefief, M.M. Thackeray, Electrochem. Commun. 9 (2007) 787.
[19] Y. Wu, A. Manthiram, Electrochem. Solid State Lett. 9 (2006) A221.
[20] X.J. Guo, Y.X. Li, M. Zheng, J.M. Zheng, J. Li, Z.L. Gong, Y. Yang, J. Power Sources 184 (2008) 414.
[21] J. Liu, Q.Y. Wang, B. Reeja-Jayan, A. Manthiram, Electrochem. Commun. 12 (2010) 750.
[22] S.-H. Kang, P. Kempgens, S. Greenbaum, A.J. Kropf, K. Amine, M.M. Thackeray, J. Mater. Chem. 17 (2007) 2069.
[23] S.J. Jin, K.S. Park, M.H. Cho, C.H. Song, A.M. Stephan, K.S. Nahm, Solid State Ionics 177 (2006) 105.
[24] S.H. Kang, K. Amine, J. Power Sources 146 (2005) 654.
[25] J.M. Amarilla, R.M. Rojas, F. Pico, L. Pascual, K. Petrov, D. Kovacheva, M.G. Lazarraga, I. Lejona, J.M. Rojo, J. Power Sources 174 (2007) 1212.
[26] D. Kovacheva, H. Gadjov, K. Petrov, S. Mandal, M.G. Lazarraga, L. Pascual, J.M. Amarilla, R.M. Rojas, P. Herrero, J.M. Rojo, J. Mater. Chem. 12 (2002) 1184.
[27] S.J. Shi, J.P. Tu, Y.Y. Tang, Y.X. Yu, Y.Q. Zhang, X.L. Wang, C.D. Gu, J. Power Sources 228 (2013) 14.
[28] P. Afanasiev, C. Geantet, Coord. Chem. Rev. 178–180 (1998) 1725.
[29] H.Y. Liang, X.P. Qiu, S.C. Zhang, Z.Q. He, W.T. Zhu, L.Q. Chen, Electrochem. Commun. 6 (2004) 505.
[30] Y. Kim, ACS Appl. Mater. Interfaces 4 (2012) 2329.
[31] W.P. Tang, X.J. Yang, Z.H. Liu, S.J. Kasaishi, K. Ooi, J. Mater. Chem. 12 (2002) 2991.
[32] K. Dua, Z.D. Peng, G.R. Hu, Y.N. Yang, L. Qi, J. Alloys Compd. 476 (2009) 329.
[33] Z.Y. Chen, W. Zhu, H.L. Zhu, J.L. Zhang, Q.F. Li, Trans. Nonferrous Met. Soc. China 20 (2010) 809.
[34] M. Helan, L.J. Berchmans, A.Z. Hussain, Ionics 16 (2010) 227.

[35] S.-H. Kang, C.S. Johnson, J.T. Vaughey, K. Amine, M.M. Thackeray, J. Electrochem. Soc. 153 (2006) A1186.
[36] X. Zhao, Y.J. Cui, L. Xiao, H.X. Liang, H.X. Liu, Solid State Ionics 192 (2011) 321.
[37] J.S. Kim, C.S. Johnson, J.T. Vaughey, M.M. Thackeray, S.A. Hackney, W. Yoon, C.P. Grey, Chem. Mater. 16 (2004) 1996.
[38] W.S. Yoon, S. Iannopollo, C.P. Grey, D. Carlier, J. Gorman, J. Reed, G. Ceder, Electrochem. Solid State Lett. 7 (2004) A167.
[39] S.H. Kang, M.M. Thackeray, C.S. Johnson, J.T. Vaughey, S.A. Hackney, Electrochem. Commun. 8 (2006) 1531.
[40] C.X. Cheng, L. Tan, H.W. Liu, X.T. Huang, Mater. Res. Bull. 46 (2011) 2032.
[41] J. Zheng, S.N. Deng, Z.C. Shi, H.J. Xu, H. Xu, Y.F. Deng, Z. Zhang, G.H. Chen, J. Power Sources 221 (2013) 108.
[42] M.M. Thackeray, S.H. Kang, C.S. Johnson, J.T. Vaughey, R. Benedek, S.A. Hackney, J. Mater. Chem. 17 (2007) 3112.
[43] C.S. Johnson, N. Li, C. Lefief, J.T. Vaughey, M.M. Thackeray, Chem. Mater. 20 (2008) 6095.
[44] W. He, J.F. Qian, Y.L. Cao, X.P. Ai, H.X. Yang, RSC Adv. 2 (2012) 3423.
[45] A. Ito, D. Li, Y. Sato, M. Arao, M. Watanabe, M. Hatano, H. Horie, Y. Ohsaw, J. Power Sources 195 (2010) 567.
[46] J. Park, J.H. Seo, G. Plett, W. Lu, A.M. Sastry, Electrochem. Solid-State Lett. 14 (2011) A14.
[47] D.H. Jang, Y.J. Shin, S.M. Oh, J. Electrochem. Soc. 143 (1996) 2204.
[48] M. Wohlfahrt-Mehrens, C. Vogler, J. Garche, J. Power Sources 127 (2004) 58.
[49] H. Chen, X. Qiu, W. Zhu, P. Hagenmuller, Electrochem. Commun. 4 (2002) 488.
[50] S.K. Martha, J. Nanda, G.M. Veith, N.J. Dudney, J. Power Sources 199 (2012) 220.
[51] H.H. Hayley, N. Yabuuchi, Y.S. Meng, S. Kumar, J. Breger, C.P. Grey, Y. Shao-Horn, Chem. Mater. 19 (2007) 2551.
[52] S.K. Hu, G.H. Cheng, M.Y. Cheng, B.J. Hwang, R. Santhanam, J. Power Sources 188 (2009) 564.
[53] Z. Li, F. Du, X.F. Bie, J. Phys. Chem. C 114 (2010) 22751.
[54] M. Park, X.C. Zhang, M. Chung, G.B. Less, A.M. Sastry, J. Power Sources 195 (2010) 7904.
[55] K.M. Shaju, G.V.S. Rao, B.V.R. Chowdariz, J. Electrochem. Soc. 151 (2004) A1324.